Surface Chemistry Hot Paper

How to cite: *Angew. Chem. Int. Ed.* **2022,** *61,* e202202127
International Edition: doi.org/10.1002/anie.202202127
German Edition: doi.org/10.1002/ange.202202127

Growth of N-Heterocyclic Carbene Assemblies on Cu(100) and Cu(111): From Single Molecules to Magic-Number Islands

Juan J. Navarro, Mowpriya Das, Sergio Tosoni, Felix Landwehr, Maximilian Koy, Markus Heyde,* Gianfranco Pacchioni, Frank Glorius,* and Beatriz Roldan Cuenya*

Abstract: N-Heterocyclic carbenes (NHCs) have superior properties as building blocks of self-assembled monolayers (SAMs). Understanding the influence of the substrate in the molecular arrangement is a fundamental step before employing these ligands in technological applications. Herein, we study the molecular arrangement of a model NHC on Cu(100) and Cu(111). While mostly disordered phases appear on Cu(100), on Cu(111) well-defined structures are formed, evolving from magic-number islands to molecular ribbons with coverage. This work presents the first example of magic-number islands formed by NHC assemblies on flat surfaces. Diffusion and commensurability are key factors explaining the observed arrangements. These results shed light on the molecule-substrate interaction and open the possibility of tuning nanopatterned structures based on NHC assemblies.

Introduction

N-Heterocyclic carbenes (NHCs) have attracted the attention of the scientific community in the last years due to their excellent properties as surface modifiers with various applications in materials science and catalysis.[1] A prime example for an application in materials science is the growth of thermally and chemically stable self-assembled monolayers (SAMs) on metallic surfaces.[2] Due to the strong NHC-metal bond, these ligands are also extensively used in other fields of materials chemistry, for example to modify and protect nanoparticles,[3] nanoelectronic devices[4] or biosensors.[5]

In order to take advantage of the benefits of NHCs in the different fields of nanotechnology, it is crucial to develop a fundamental understanding of the interaction of these molecules with different model metal surfaces. NHCs have been employed for the functionalization of various nanoparticles based on different metals.[6] In contrast, the adsorption of NHCs on flat surfaces has been so far mainly studied on gold,[5a,7] with only a few works carried out on other metals such as copper,[7k,8] silver[8b,9] or platinum.[10] The adsorption on silicon flat surfaces was also reported.[11] With a few exceptions,[7i] these works are limited to (111) facets, which gives only a partial vision of the molecular self-assembly and misses the description of diffusion mechanisms on other facets. In addition, abundant and inexpensive first row transition metals receive increasing attention and a detailed mechanistic understanding is crucial for prospective applications of these promising surfaces in materials science and catalysis.[12]

Herein we explore the growth of molecular films on Cu(100) and Cu(111) under ultra high vacuum (UHV) conditions using a model NHC, 1,3-bis(2,6-diisopropylphenyl)imidazol-2-ylidene (IPr-NHC, Scheme 1c), by means of low-temperature (5 K) scanning tunneling microscopy (STM) and density functional theory (DFT). A model NHC with isopropyl substituent groups was previously deposited on Cu(111) by Larrea et al.[8a] The authors reported a high molecular mobility during STM measurements at 300 K, hindering the observation of any kind of ordered structures. The low-temperature STM measurements carried out in the present study reveal the arrangement of IPr-NHC on Cu(100) and Cu(111), contributing to the understanding of the self-assembly mechanisms taking place on copper surfaces. In combination with DFT calculations, adsorption modes and diffusion mechanisms are investigated.

Results and Discussion

Deposition of IPr-NHC molecules on Cu(100) at low coverage and with the sample at 310 K, results in a dispersed

[*] Dr. J. J. Navarro, F. Landwehr, Dr. M. Heyde, Prof. Dr. B. Roldan Cuenya
Fritz-Haber Institute of the Max Planck Society, Department of Interface Science
Faradayweg 4–6, 14195 Berlin (Germany)
E-mail: heyde@fhi.mpg.de

M. Das, Dr. M. Koy, Prof. Dr. F. Glorius
Westfälische Wilhelms-Universität, Organisch-Chemisches Institut
Corrensstraße 40, 48149 Münster (Germany)
E-mail: glorius@uni-muenster.de

Dr. S. Tosoni, Prof. Dr. G. Pacchioni
Dipartimento di Scienza dei Materiali, Università di Milano-Bicocca
Via Cozzi 55, 20125 Milano (Italy)
E-mail: sergio.tosoni@unimib.it

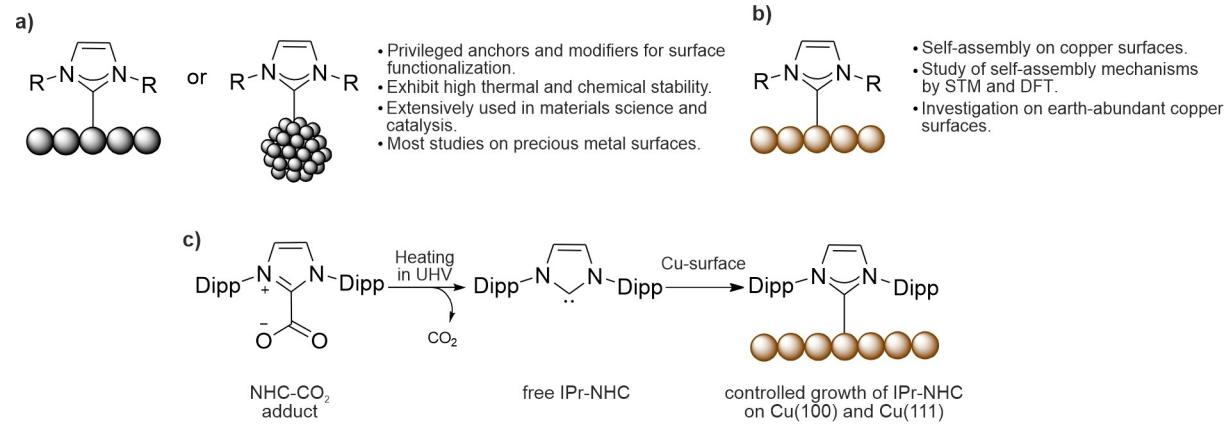

Scheme 1. NHCs on metal surfaces. a) Flat surfaces and nanoparticles. b) The scope of this work is the adsorption of NHCs on copper planar surfaces: Cu(100) and Cu(111). c) Schematic illustration of the deposition of free IPr-NHC on Cu(100) and Cu(111) under UHV conditions. Dipp: 2,6-diisopropylphenyl.

arrangement where single molecules, dimers and other larger structures can be observed, as shown in Figure 1a. In contrast, for the same coverage and deposition conditions, IPr-NHC on Cu(111) leads to the formation of nanoislands with well-defined shapes, that are homogeneously distributed along the surface, Figure 1b. These molecular nanoislands avoid the surface steps and stay separated from neighboring islands. The upper steps of the terraces are decorated by the ligands, forming a 1D chain. This feature has also been observed for other NHC molecules on Au(111).[7j] A higher coverage of IPr-NHC on Cu(100) leads to some molecular patches, exhibiting an arrangement in close packed configuration (Figure 1c). The space between the patches resembles the arrangement observed for lower IPr-NHC coverages, with heterogeneous structures and a relatively high amount of isolated molecules. The same deposition conditions on Cu(111) lead to the formation of large molecular domains, growing along three directions, with a well-defined molecular arrangement. Moreover, the film exhibits trenches, as a consequence of the growth along preferential directions, which are populated occasionally by diffusing single molecules. The thermal stability of these structures is discussed in Section 11 of the Supporting Information. Although the arrangement on both surfaces presents clear differences, both the patches formed at large coverage on Cu(100) and the molecular lattice obtained for low and high coverage on Cu(111) present a hexagonal lattice with a molecule-molecule distance of 1.2 ± 0.1 nm. This fact indicates that the short-range order is dominated by intermolecular interactions on both substrates. However, the different long-range appearance suggests a significant influence of the molecule-substrate interaction.

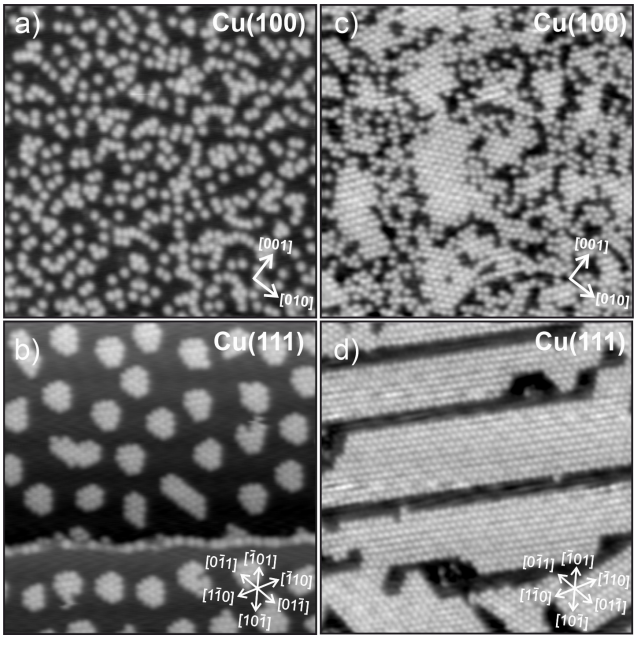

Figure 1. IPr-NHC deposited on Cu(100) and Cu(111) at different coverages. Large differences in the long-range arrangement between the two substrates can be observed. 0.25 ML deposition on a) Cu(100), b) Cu(111). 0.75 ML deposition on c) Cu(100) and d) Cu(111). Imaging conditions: 50 nm × 50 nm, $V_s = +1.5$ V, $I_t = 20$ pA.

A more detailed structural analysis sheds light on the influence of the crystallographic orientation of the substrate in the molecular arrangement. Figure 2a displays a larger area on Cu(100) showing the mentioned molecular patches, which can be classified in two rotational domains. Figure 2b shows two patches, each corresponding to a different rotational domain, separated by smaller structures without a well-defined arrangement. The domains are rotated ca. 30° with respect to each other, aligning one of the axis of the molecular lattice with one of the high symmetry directions of Cu(100). The fast Fourier transform (FFT) in Figure 2c was obtained from the STM image of Figure S1a, which shows a large representative area of the surface. The two rotational domains can be barely distinguished, indicating a low degree of order in the organic film. Figure 2d shows a model of the molecular lattice found in the patches. The resulting structure can be described as $\frac{\sqrt{21}}{2}\begin{pmatrix} 0 & 2 \\ \sqrt{3} & 1 \end{pmatrix}$, and is non-commensurate with the Cu(100) lattice.

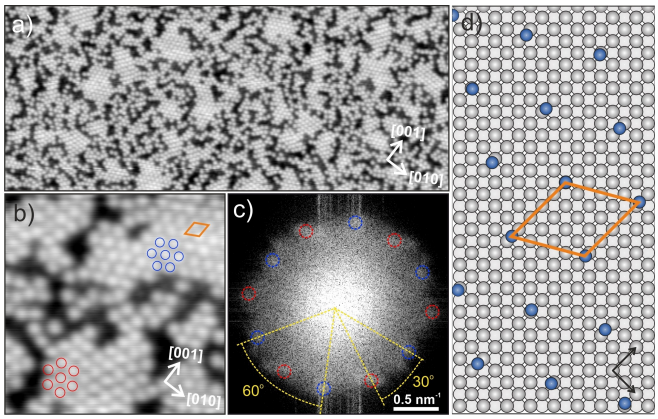

Figure 2. Analysis of the arrangement of IPr-NHC on Cu(100). a) 120 nm×50 nm, $V_s = +1.5$ V, $I_t = 50$ pA, b) 18 nm×18 nm, $V_s = +1.5$ V, $I_t = 50$ pA, c) FFT of the STM image shown in Figure S1a, d) ball model for the arrangement of IPr-NHC on Cu(100). Molecular unit cell marked in orange, and rotational domains in blue and red. High symmetry directions of Cu(100) are marked by arrows.

A high coverage of IPr-NHC on Cu(111) leads to the formation of molecular ribbons that extend along large areas, as shown in Figure 3a. Similar structures were observed on Au(111) as a consequence of the confinement of the molecules in the herringbone reconstruction.[7d] In contrast, there is not such a reconstruction on Cu(111), where the substrate guides the formation of molecular ribbons along preferential directions. The resulting organic film generates in this way a molecular nanopattern of the surface. This arrangement presents two rotational domains, which are indicated in Figure 3b. These domains are rotated $22 \pm 1°$ with respect to each other and $11 \pm 1°$ with respect to the high symmetry directions of Cu(111). Sharp spots corresponding to the IPr-NHC molecular lattice appear in the FFT shown in Figure 3c. The sharpness of the FFT spots

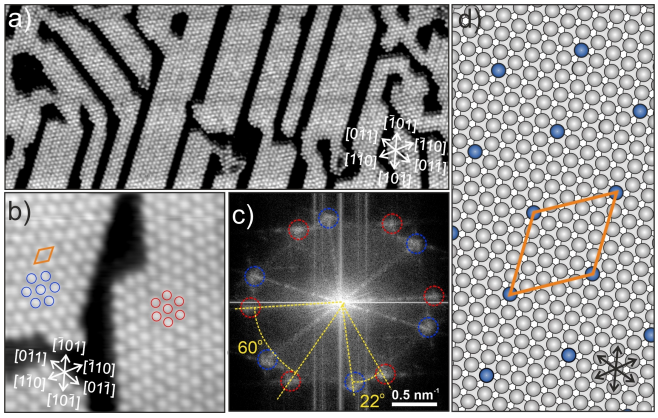

Figure 3. Analysis of the arrangement of IPr-NHC on Cu(111). a) 120 nm×50 nm, $V_s = +1.0$ V, $I_t = 20$ pA, b) 18 nm×18 nm, $V_s = +2.0$ V, $I_t = 100$ pA, c) FFT of the STM image shown in Figure S1c, d) ball model for the arrangement of IPr-NHC on Cu(111). Molecular unit cell marked in orange, rotational domains in blue and red. High symmetry directions of Cu(111) are marked by arrows.

is a consequence of the high degree of order in the film. In contrast to Cu(100), the FFT related to the arrangement of IPr-NHC on Cu(111) clearly shows only two rotational domains. The ball model of Figure 3d represents the resulting molecular lattice, which is in this case commensurate with the substrate and can be described as $\sqrt{21} \times \sqrt{21}$ R11°.

DFT calculations were carried out in order to get insight into the adsorption modes of IPr-NHC on Cu(100) and Cu(111). On Cu(100), the calculations predict mainly two adsorption modes: on-top and bridge. On both cases, the molecule is in upright configuration. Figure 4a and b show the IPr-NHC in bridge position, where the carbene center is bound to two surface Cu atoms, with an adsorption energy of −4.2 eV. The C–Cu bond lengths are 2.0 Å and 2.3 Å. A slight protrusion of the binding Cu atom is observed (≈0.1 Å). The on-top configuration, shown in Figure 4c and d presents a similar adsorption energy of −4.1 eV. The carbene center is bound to a Cu atom with a C–Cu bond of 2.0 Å and the central molecular ring is almost orthogonal to the surface. The binding Cu atom is uplifted by 0.3 Å. On

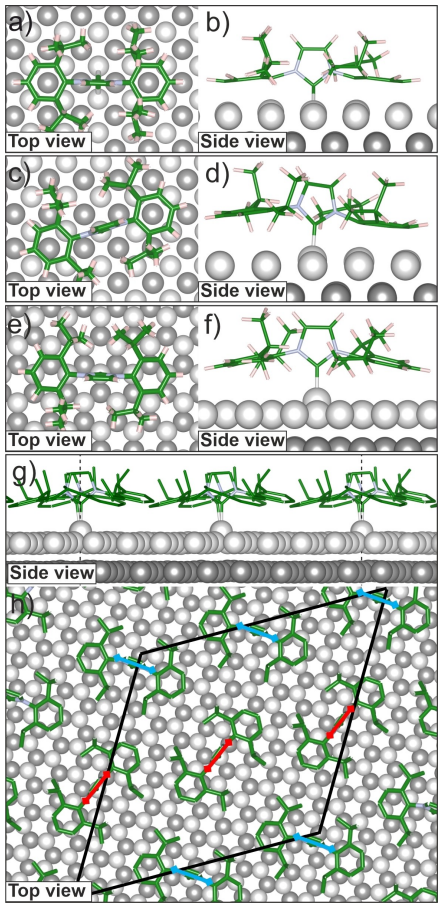

Figure 4. Adsorption configuration of IPr-NHC simulated by DFT. On Cu(100): a) Top and b) side views of bridge configuration, and c) top, d) side views of on-top configuration. On Cu(111): e) Top and f) side views of on-top configuration; g) side and h) top views of a molecular array. Red and blue arrows highlight the different orientations of the molecules in the array. Unit cell marked in black.

Cu(111), the most stable adsorption mode is the on-top configuration with the molecule in upright position, shown in Figure 4e and f, where the carbene center binds to a surface Cu atom with a C–Cu bond length of 2.0 Å, causing a remarkable uplift of the Cu atom of 0.7 Å. The central ring lies perpendicular with respect to the surface, while the phenyl rings of the substituents interact through dispersive forces with the copper substrate. The adsorption energy in this configuration is −3.7 eV, being the rotation along the axis normal to the surface allowed. This binding mode exhibits similar features to what was reported for the same ligand on Au(111), where the reported adsorption energy is −2.8 eV and the displacement of the Au atom bound to the IPr-NHC is 0.6 Å.[7e] As expected, the adsorption energy is higher on Cu(111).

The self-assembly of IPr-NHC on Cu(111) was also simulated by locating a layer of adsorbed molecules on the surface following the distribution experimentally detected (as shown in Figure 3d). A double supercell is also adopted in order to allow the reciprocal rotation of the first neighbours within the assembled molecules. By performing a scan of various possible orientations, the most stable configuration was identified, resulting in the structure shown in Figure 4g and h. In this model, the molecules present two different orientations, differing 59° with respect to each other. Under these conditions, the adsorption energy decreases slightly to −3.5 eV, while the distance with respect to the surface of the binding Cu atoms increases reaching 0.8 Å. Notably, in the case of Cu(100), the loss of adsorption energy upon assembly of the ligand at a comparable density is almost 25 %. These observations suggest a change of the C–Cu bond length according to the molecular coverage and, therefore, a way of tuning the molecule-substrate interaction.

In order to extend our understanding about the differences in the long-range arrangement of IPr-NHC on Cu(100) and Cu(111), a number of surface diffusion processes were analyzed by means of nudged elastic band calculations. Table 1 collects the thermodynamic and kinetic parameters for the considered diffusion mechanisms. One of the possibilities that were taken into account is a ballbot-type motion, as reported for IPr-NHC on Au(111) by Wang et al.[7d] The creation of a surface vacancy to generate a mobile extra-lattice Cu atom adsorbed on a hollow site in either Cu(100) or Cu(111) is not expected under the described experimental conditions due to the large thermodynamic cost (1.2 eV for Cu(100) and 1.8 eV for Cu(111)). However, the presence of IPr-NHC molecules reduces the energy barriers dramatically, enabling the formation of Cu adatoms bound to the ligands in a ballbot configuration. In the case of the closed-packed Cu(111), the enabling role played by the ligand is more pronounced compared to Cu(100), reducing the thermodynamic and kinetic barrier for the uptake of a Cu atom by 60 % and 50 % respectively. The kinetic barrier is even lower for Au(111).[7d] The diffusion barriers through this mechanism are relatively low, resulting in 0.36 eV on Cu(100) and 0.12 eV on Cu(111). Another diffusion process has been considered, where the ligand is desorbed from a surface site and readsorbed on another nearby equivalent site, without displacing any Cu atom. This desorption/readsorption path has small diffusion barriers both on Cu(111), 0.31 eV, and on Cu(100), 0.49 eV.

Table 1: Thermodynamic and kinetic aspects of the diffusion of IPr-NHC on Cu(100) and Cu(111) obtained by DFT calculations: energy difference between final and initial state (ΔE, eV), kinetic barriers (ΔE^k, eV) and mean residence time (t, s). t was calculated from the attempt-to-jump frequency, Γ, being $\Gamma = \Gamma_o e^{\frac{-\Delta E^k}{k_B T}}$, $\Gamma_o = 10$ THz, $T = 343$ K, $t = \frac{1}{\Gamma}$. Kinetic barriers related to IMe-NHC on Au(111) as presented in the work by Wang et al.[7d] are also included for comparison.

Surface	Process	ΔE [eV]	ΔE^k [eV]	t [s]
Cu(100)	Adatom formation	1.21	1.48	5.0×10^{8}
	Adatom diffusion	0.00	0.40	7.0×10^{-8}
	Ballbot formation	0.75	1.04	1.7×10^{2}
	Ballbot diffusion	0.03	0.36	2.1×10^{-8}
	Desorption/adsorption	0.00	0.49	1.6×10^{-6}
Cu(111)	Adatom formation	1.81	1.98	1.3×10^{16}
	Adatom diffusion	0.03	0.07	2.4×10^{-13}
	Ballbot formation	0.74	0.98	28.1
	Ballbot diffusion	0.09	0.12	6.0×10^{-12}
	Desorption/adsorption	0.00	0.31	2.6×10^{-9}
Au(111) [a]	Adatom formation		1.30	
	Adatom diffusion		0.10	
	Ballbot formation		0.12	
	Ballbot diffusion		0.10	
	Desorption/adsorption		0.80	

[a] Data from the work by Wang et al.[7d]

Although the presented data do not indicate a strong preference for a ballbot motion or a desorption/readsorption mechanism, the kinetic barriers are in both cases higher for Cu(100) than for Cu(111), by a factor of 3 or ≈1.6, respectively. This observation is in agreement with a higher molecular mobility observed on Cu(111) during STM measurements (see Section 10 of the Supporting Information). The size distribution of the molecular clusters at low coverage also evidences this difference. Figure 5a is a STM image showing a large area with 0.25 ML of IPr-NHC on Cu(100). The ligands arrange in a variety of structures composed of a different number of molecules. Figure 5b displays the size distribution of the observed molecular clusters. Almost half of the molecules are adsorbed individually on the surface, followed by around a quarter of dimers. The rest of ligands form larger structures, whose size is rarely above 10 molecules. A completely different scenario occurs for the same coverage on Cu(111). Figure 5c shows well-defined nanoislands that are homogeneously distributed along the surface. In addition, certain sizes and shapes seem to be preferred. According to the distribution of sizes, shown in Figure 5d, more than half of the islands are composed of 12 members. Furthermore, the size distribution is centered on 12, with monomers or dimers only appearing on rare occasions, in contrast with the distribution of Figure 5b for Cu(100). On the other hand, the size distribution of Figure 5d changes after annealing treatments (Section 11 of the Supporting Information) and depends on the temperature at which the STM measurements are taken (Section 12 of the Supporting Information).

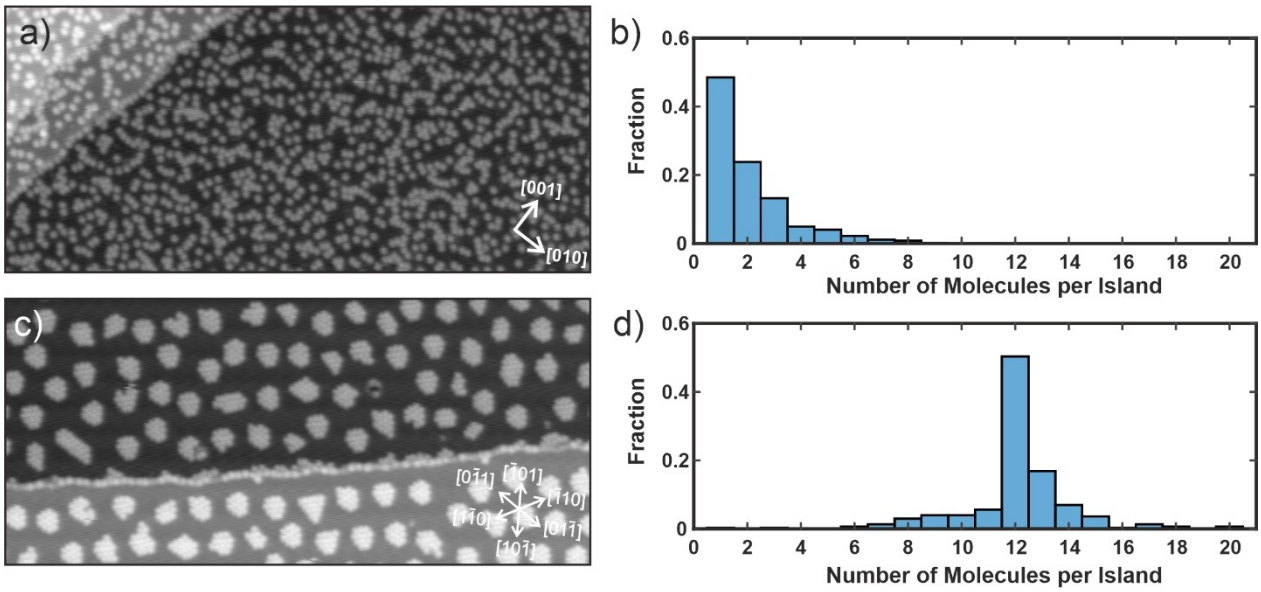

Figure 5. Cluster formation of IPr-NHC on Cu(100) and Cu(111) at low coverage. a) 0.25 ML coverage on Cu(100). 120 nm × 55 nm, $V_s = +1.5$ V, $I_t = 20$ pA. b) Histogram representing the sizes of molecular clusters found in STM images like that shown in Figure S7a, corresponding with a 0.25 ML coverage on Cu(100). c) 0.25 ML coverage on Cu(111). 120 nm × 55 nm, $V_s = +1.5$ V, $I_t = 20$ pA. d) Histogram representing the sizes of molecular clusters found in STM images as shown in Figure S7b, corresponding with a 0.25 ML coverage on Cu(111). High symmetry directions of the substrate are marked by arrows.

Up to this point, we showed that the Cu(100) surface presents higher diffusion barriers and makes difficult the formation of a well ordered IPr-NHC lattice due to lack of commensurability. These two ideas are in agreement with the size distribution of Figure 5b. In the case of Cu(111), we demonstrated that this surface provides lower diffusion barriers and allows the formation of a IPr-NHC lattice, which is commensurate with respect to the substrate. However, these properties would lead to a continuous molecular layer instead of the size distribution shown in Figure 5d. In order to solve this paradox, DFT calculations were employed to evaluate the strain in the molecular lattice on both substrates. In particular, we simulated a free-standing molecular lattice and evaluated the mismatch with respect to the Cu(100) and Cu(111) surfaces (Section 6 of the Supporting Information). The mismatch along the vectors of the molecular unit cell and the angle between unit cell vectors are collected in Table 2. On Cu(100) the strain is biaxial and large on both directions. Moreover, the coincidence of the molecular position with the Cu sites is poor, as expected. Surprisingly, the IPr-NHC lattice on Cu(111) coincides very well with the substrate along one of the directions, but presents a significant compressive strain along the other direction. This uniaxial strain explains the formation of elongated structures on Cu(111) as the coverage increases (Section 7 of the Supporting Information). It is also in agreement with the formation of islands at low coverages, which is a necessary arrangement in order to diminish the surface energy.

Table 2: Relaxed lattice parameters of the free-standing molecular lattice and mismatch with Cu(100) and Cu(111).

		a [Å]	b [Å]	γ [°]
Cu(100)	Mol. lattice	23.16	20.56	−2.8
	Cu(100)	21.42	21.42	90.0
	Strain [%]	−8.1%	+4.0%	−3.1%
Cu(111)	Mol. lattice	23.16	24.17	121.6
	Cu(111)	23.14	23.14	120.0
	Strain [%]	−0.1%	−4.4%	−1.3%

The size distribution of these islands reveal also an intriguing characteristic. Figure 6 shows the size distribution for different coverages: 0.05, 0.15, 0.25 and 0.35 ML. For 0.05 ML, the triangular three-membered islands (orange) and the hexagonal seven-membered islands (blue) are the most frequent configurations following the symmetry of the hexagonal molecular lattice. There is one structure that predominates for 0.15, 0.25 and 0.35 ML: the threefold 12-membered island (green). This magic-number island seems to be a favored configuration in this range of coverages, especially for 0.25 ML, where almost half of the islands exhibit this structure. Assuming a ballbot configuration, the molecules could arrange on Cu(111) like Cu adatoms driven by the influence of the surface state,[13] but this hypothesis does not match our observations (Section 9 of Supporting Information). Moiré superstructures can also mediate the growth of islands with specific shapes and sizes.[14] The intermolecular interactions play in any case a key role in the formation of magic-number molecular islands on surfaces. Van der Waals attraction, hydrogen bonds, Coulomb repulsion, dipole interaction or metal-organic coordination have been probed to play a key role in supramolecular self-assemblies leading to magic-number islands.[15] For example,

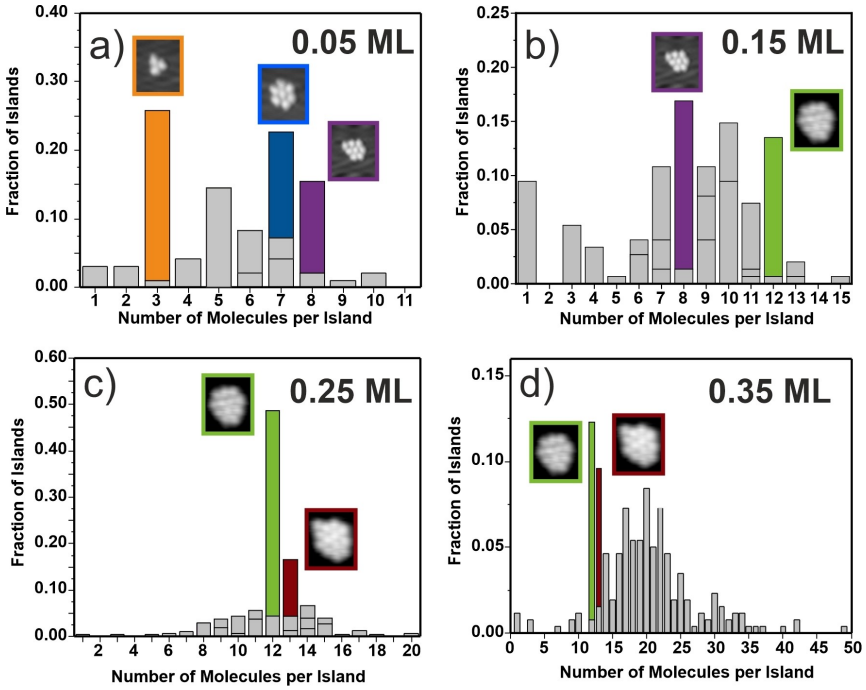

Figure 6. Histograms representing the size distribution of the molecular islands appearing on Cu(111) at different coverages: a) 0.05 ML, b) 0.15 ML, c) 0.25 ML and d) 0.35 ML. The formation of magic-number islands can be observed. Data obtained from STM images like those shown in Figure S6.

CH-π interactions were reported to drive the self-assembly of phenylacetylene molecules on Au(111), leading to well defined hexamers.[16] This kind of interaction seems to be also relevant in the self-assembly of NHCs containing isopropyl groups.[7j] For the reported IPr-NHC, the presence of phenyl rings and isopropyl groups could then produce attractive intermolecular interactions, which would be responsible for the hexagonal molecular lattice on both Cu(100) and Cu(111).

On Cu(111), the uniaxial strain induces the formation of islands at low coverages. As explained in Section 7 of the Supporting Information, the island edge tension[17] may favor the shapes exhibiting the symmetry of the molecular lattice. At higher coverages, the uniaxial strain becomes more relevant for the self-assembly, leading to elongated structures. Figure 6 suggests that the threefold 12-membered island represents an optimal edge tension preceding the formation of elongated structures. This could be the reason why these magic-number islands dominate even at 0.35 ML, where already much larger and elongated structures can be formed. A reorientation of the molecules at the edge of the number-magic islands could also have an effect on the observed size distribution. This reorientation might be key to guide the molecular growth process and is an interesting aspect for further STM measurements and challenging DFT calculations.

Conclusion

The arrangement of IPr-NHC on Cu(100) and Cu(111) presents important differences. On Cu(100) the molecules do not display well ordered structures until the coverage is high enough to form small closed-packed patches. On Cu(111) well defined structures appear already at low coverages. We described the influence of the substrate in the molecular arrangement, taking into consideration diffusion, commensurability and strain. On Cu(100) the formed closed-packed patches are not commensurate with the substrate and exhibit a large strain. In addition, the diffusion barriers are higher than on Cu(111). On the Cu(111) surface, the molecular lattice formed is commensurate with respect to the substrate and presents a compressive uniaxial strain, which may explain the structures formed as the coverage increases, going from discrete islands to molecular ribbons.

In particular, the threefold 12-membered island presents the optimal size and shape preceding the formation of elongated structures. Further work should be carried out in the future to obtain a more quantitative understanding of the growth process of these magic-number islands and the transition towards elongated structures. Increasing the understanding of growth processes will help the design of tailormade molecular NHC assemblies with nanopatterned structures for diverse applications.

Acknowledgements

Generous financial support of the Deutsche Forschungsgemeinschaft (SFB 858) and the Alexander von Humboldt Foundation (J.J.N.) is gratefully acknowledged. S.T. and G.P. acknowledge the financial support from the Italian Ministry of University and Research (MIUR) through the PRIN Project 20179337R7, and the grant Dipartimenti di Eccellenza-2017 "Materials For Energy". Access to the CINECA supercomputing resources was granted via IS-CRAB. Open Access funding enabled and organized by Projekt DEAL.

Conflict of Interest

The authors declare no conflict of interest.

Data Availability Statement

The data that support the findings of this study are available from the corresponding author upon reasonable request.

Keywords: Density Functional Calculations · Magic-Number Islands · Molecular Self-Assembly · N-Heterocyclic Carbenes · Scanning Tunneling Microscopy

[1] a) D. Bourissou, O. Guerret, F. P. Gabbaï, G. Bertrand, *Chem. Rev.* **2000**, *100*, 39–92; b) M. N. Hopkinson, C. Richter, M. Schedler, F. Glorius, *Nature* **2014**, *510*, 485–496; c) P. Bellotti, M. Koy, M. N. Hopkinson, F. Glorius, *Nat. Chem. Rev.* **2021**, *5*, 711–725.

[2] a) A. V. Zhukhovitskiy, M. J. MacLeod, J. A. Johnson, *Chem. Rev.* **2015**, *115*, 11503–11532; b) C. A. Smith, M. R. Narouz, P. A. Lummis, I. Singh, A. Nazemi, C.-H. Li, C. M. Crudden, *Chem. Rev.* **2019**, *119*, 4986–5056; c) M. Koy, P. Bellotti, M. Das, F. Glorius, *Nat. Catal.* **2021**, *4*, 352–363.

[3] a) E. C. Hurst, K. Wilson, I. J. S. Fairlamb, V. Chechik, *New J. Chem.* **2009**, *33*, 1837–1840; b) J. Vignolle, T. D. Tilley, *Chem. Commun.* **2009**, 7230–7232; c) K. V. S. Ranganath, J. Kloesges, A. H. Schäfer, F. Glorius, *Angew. Chem. Int. Ed.* **2010**, *49*, 7786–7789; *Angew. Chem.* **2010**, *122*, 7952–7956; d) K. Salorinne, R. W. Y. Man, C.-H. Li, M. Taki, M. Nambo, C. M. Crudden, *Angew. Chem. Int. Ed.* **2017**, *56*, 6198–6202; *Angew. Chem.* **2017**, *129*, 6294–6298.

[4] E. A. Doud, M. S. Inkpen, G. Lovat, E. Montes, D. W. Paley, M. L. Steigerwald, H. Vázquez, L. Venkataraman, X. Roy, *J. Am. Chem. Soc.* **2018**, *140*, 8944–8949.

[5] a) C. M. Crudden, J. H. Horton, M. R. Narouz, Z. Li, C. A. Smith, K. Munro, C. J. Baddeley, C. R. Larrea, B. Drevniok, B. Thanabalasingam, A. B. McLean, O. V. Zenkina, I. I. Ebralidze, Z. She, H.-B. Kraatz, N. J. Mosey, L. N. Saunders, A. Yagi, *Nat. Commun.* **2016**, *7*, 12654; b) I. Singh, D. S. Lee, S. Huang, H. Bhattacharjee, W. Xu, J. F. McLeod, C. M. Crudden, Z. She, *Chem. Commun.* **2021**, *57*, 8421–8424.

[6] a) E. A. Baquero, S. Tricard, J. C. Flores, E. de Jesús, B. Chaudret, *Angew. Chem. Int. Ed.* **2014**, *53*, 13220–13224; *Angew. Chem.* **2014**, *126*, 13436–13440; b) J. B. Ernst, S. Muratsugu, F. Wang, M. Tada, F. Glorius, *J. Am. Chem. Soc.* **2016**, *138*, 10718–10721; c) J. B. Ernst, C. Schwermann, G.-i. Yokota, M. Tada, S. Muratsugu, N. L. Doltsinis, F. Glorius, *J. Am. Chem. Soc.* **2017**, *139*, 9144–9147; d) R. Ye, A. V. Zhukhovitskiy, R. V. Kazantsev, S. C. Fakra, B. B. Wickemeyer, F. D. Toste, G. A. Somorjai, *J. Am. Chem. Soc.* **2018**, *140*, 4144–4149; e) N. Kaeffer, H.-J. Liu, H.-K. Lo, A. Fedorov, C. Copéret, *Chem. Sci.* **2018**, *9*, 5366–5371; f) R. W. Y. Man, C.-H. Li, M. W. A. MacLean, O. V. Zenkina, M. T. Zamora, L. N. Saunders, A. Rousina-Webb, M. Nambo, C. M. Crudden, *J. Am. Chem. Soc.* **2018**, *140*, 1576–1579; g) M. R. Narouz, K. M. Osten, P. J. Unsworth, R. W. Y. Man, K. Salorinne, S. Takano, R. Tomihara, S. Kaappa, S. Malola, C.-T. Dinh, J. D. Padmos, K. Ayoo, P. J. Garrett, M. Nambo, J. H. Horton, E. H. Sargent, H. Häkkinen, T. Tsukuda, C. M. Crudden, *Nat. Chem.* **2019**, *11*, 419–425; h) N. Kaeffer, D. Mance, C. Copéret, *Angew. Chem. Int. Ed.* **2020**, *59*, 19999–20007; *Angew. Chem.* **2020**, *132*, 20174–20182.

[7] a) T. Weidner, J. E. Baio, A. Mundstock, C. Große, S. Karthäuser, C. Bruhn, U. Siemeling, *Aust. J. Chem.* **2011**, *64*, 1177–1179; b) A. V. Zhukhovitskiy, M. G. Mavros, T. V. Voorhis, J. A. Johnson, *J. Am. Chem. Soc.* **2013**, *135*, 7418–7421; c) H. K. Kim, A. S. Hyla, P. Winget, H. Li, C. M. Wyss, A. J. Jordan, F. A. Larrain, J. P. Sadighi, C. Fuentes-Hernandez, B. Kippelen, J.-L. Brédas, S. Barlow, S. R. Marder, *Chem. Mater.* **2017**, *29*, 3403–3411; d) G. Wang, A. Rühling, S. Amirjalayer, M. Knor, J. B. Ernst, C. Richter, H.-J. Gao, A. Timmer, H.-Y. Gao, N. L. Doltsinis, F. Glorius, H. Fuchs, *Nat. Chem.* **2017**, *9*, 152–156; e) A. Bakker, A. Timmer, E. Kolodzeiski, M. Freitag, H. Y. Gao, H. Mönig, S. Amirjalayer, F. Glorius, H. Fuchs, *J. Am. Chem. Soc.* **2018**, *140*, 11889–11892; f) G. Lovat, E. A. Doud, D. Lu, G. Kladnik, M. S. Inkpen, M. L. Steigerwald, D. Cvetko, M. S. Hybertsen, A. Morgante, X. Roy, L. Venkataraman, *Chem. Sci.* **2019**, *10*, 930–935; g) A. Bakker, M. Freitag, E. Kolodzeiski, P. Bellotti, A. Timmer, J. Ren, B. Schulze Lammers, D. Moock, H. W. Roesky, H. Mönig, S. Amirjalayer, H. Fuchs, F. Glorius, *Angew. Chem. Int. Ed.* **2020**, *59*, 13643–13646; *Angew. Chem.* **2020**, *132*, 13745–13749; h) J. Ren, M. Freitag, C. Schwermann, A. Bakker, S. Amirjalayer, A. Rühling, H.-Y. Gao, N. L. Doltsinis, F. Glorius, H. Fuchs, *Nano Lett.* **2020**, *20*, 5922–5928; i) S. Amirjalayer, A. Bakker, M. Freitag, F. Glorius, H. Fuchs, *Angew. Chem. Int. Ed.* **2020**, *59*, 21230–21235; *Angew. Chem.* **2020**, *132*, 21416–21422; j) A. Inayeh, R. R. K. Groome, I. Singh, A. J. Veinot, F. C. de Lima, R. H. Miwa, C. M. Crudden, A. B. McLean, *Nat. Commun.* **2021**, *12*, 4034; k) J. Ren, M. Freitag, Y. Gao, P. Bellotti, M. Das, B. S. Lammers, H. Mönig, Y. Zhang, C. G. Daniliuc, S. Du, H. Fuchs, F. Glorius, *Angew. Chem. Int. Ed.* **2022**, *61*, e202115104; *Angew. Chem.* **2022**, *134*, e202115104.

[8] a) C. R. Larrea, C. J. Baddeley, M. R. Narouz, N. J. Mosey, J. H. Horton, C. M. Crudden, *ChemPhysChem* **2017**, *18*, 3536–3539; b) L. Jiang, B. Zhang, G. Médard, A. P. Seitsonen, F. Haag, F. Allegretti, J. Reichert, B. Kuster, J. V. Barth, A. C. Papageorgiou, *Chem. Sci.* **2017**, *8*, 8301–8308; c) A. J. Veinot, A. Al-Rashed, J. D. Padmos, I. Singh, D. S. Lee, M. R. Narouz, P. A. Lummis, C. J. Baddeley, C. M. Crudden, J. H. Horton, *Chem. Eur. J.* **2020**, *26*, 11431–11434.

[9] P. Knecht, B. Zhang, J. Reichert, D. A. Duncan, M. Schwarz, F. Haag, P. T. P. Ryan, T.-L. Lee, P. S. Deimel, P. Feulner, F. Allegretti, W. Auwärter, G. Médard, A. P. Seitsonen, J. V. Barth, A. C. Papageorgiou, *J. Am. Chem. Soc.* **2021**, *143*, 4433–4439.

[10] a) Y. Zeng, T. Zhang, M. R. Narouz, C. M. Crudden, P. H. McBreen, *Chem. Commun.* **2018**, *54*, 12527–12530; b) S. Dery, I. Berg, S. Kim, A. Cossaro, A. Verdini, L. Floreano, F. D. Toste, E. Gross, *Langmuir* **2020**, *36*, 697–703.

[11] a) A. V. Zhukhovitskiy, M. G. Mavros, K. T. Queeney, T. Wu, T. V. Voorhis, J. A. Johnson, *J. Am. Chem. Soc.* **2016**, *138*, 8639–8652; b) M. Franz, S. Chandola, M. Koy, R. Zielinski, H. Aldahhak, M. Das, M. Freitag, U. Gerstmann, D. Liebig, A. K.

Hoffmann, M. Rosin, W. G. Schmidt, C. Hogan, F. Glorius, N. Esser, M. Dähne, *Nat. Chem.* **2021**, *13*, 828–835.
[12] R. M. Bullock, J. G. Chen, L. Gagliardi, P. J. Chirik, O. K. Farha, C. H. Hendon, C. W. Jones, J. A. Keith, J. Klosin, S. D. Minteer, R. H. Morris, A. T. Radosevich, T. B. Rauchfuss, N. A. Strotman, A. Vojvodic, T. R. Ward, J. Y. Yang, Y. Surendranath, *Science* **2020**, *369*, eabc3183.
[13] a) N. Knorr, H. Brune, M. Epple, A. Hirstein, M. A. Schneider, K. Kern, *Phys. Rev. B* **2002**, *65*, 115420; b) F. Silly, M. Pivetta, M. Ternes, F. Patthey, J. P. Pelz, W.-D. Schneider, *Phys. Rev. Lett.* **2004**, *92*, 016101.
[14] D. V. Gruznev, A. V. Matetskiy, L. V. Bondarenko, O. A. Utas, A. V. Zotov, A. A. Saranin, J. P. Chou, C. M. Wei, M. Y. Lai, Y. L. Wang, *Nat. Commun.* **2013**, *4*, 1679.
[15] a) M. Böhringer, K. Morgenstern, W. D. Schneider, R. Berndt, *J. Phys. Condens. Matter* **1999**, *11*, 9871–9878; b) A. D. Jewell, S. M. Simpson, A. Enders, E. Zurek, E. C. H. Sykes, *J. Phys. Chem. Lett.* **2012**, *3*, 2069–2075; c) S. Kervyn, N. Kalashnyk, M. Riello, B. Moreton, J. Tasseroul, J. Wouters, T. S. Jones, A. De Vita, G. Costantini, D. Bonifazi, *Angew. Chem. Int. Ed.* **2013**, *52*, 7410–7414; *Angew. Chem.* **2013**, *125*, 7558–7562; d) Y. Cui, Y. Pan, T. Meyer, N. Nilius, *J. Phys. Chem. C* **2017**, *121*, 4318–4323; e) X. Wan, L. Liu, Y. Zhang, X. Liu, Y. Qian, E. Kan, H. Kong, H. Fuchs, *J. Phys. Chem. C* **2021**, *125*, 358–365.
[16] Q. Li, C. Han, S. R. Horton, M. Fuentes-Cabrera, B. G. Sumpter, W. Lu, J. Bernholc, P. Maksymovych, M. Pan, *ACS Nano* **2012**, *6*, 566–572.
[17] J. Ikonomov, C. H. Schmitz, M. Sokolowski, *Phys. Rev. B* **2010**, *81*, 195428.

Manuscript received: February 8, 2022
Accepted manuscript online: April 25, 2022
Version of record online: June 10, 2022